

Localised convection cells in the presence of a vertical magnetic field

By **J. H. P. DAWES**

Department of Applied Mathematics and Theoretical Physics, Centre for Mathematical Sciences, University of Cambridge, Wilberforce Road, Cambridge, CB3 0WA, UK.

(Received 16 June 2006)

Thermal convection in a horizontal fluid layer heated uniformly from below usually produces an array of convection cells of roughly equal amplitudes. In the presence of a vertical magnetic field, convection may instead occur in vigorous isolated cells separated by regions of strong magnetic field. An approximate model for two-dimensional solutions of this kind is constructed, using the limits of small magnetic diffusivity, large magnetic field strength and large thermal forcing.

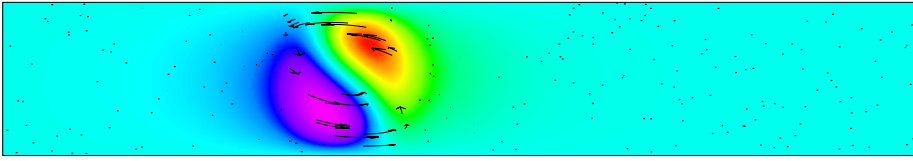
The approximate model captures the essential physics of these localised states, enables the determination of unstable localised solutions and indicates the approximate region of parameter space where such solutions exist. Comparisons with fully nonlinear numerical simulations are made, and reveal a power law scaling describing the location of the saddle node bifurcation in which the localised states disappear.

1. Introduction

A multitude of dissipative continuum systems undergo pattern-forming instabilities as the driving for the system is increased. Of these, Rayleigh–Bénard convection and its variants are of particular importance. Chandrasekhar (1961) discusses the linear theory for the Rayleigh–Bénard problem with and without a magnetic field. Nonlinear aspects of pattern formation set in the context of thermal convection are presented by Cross & Hohenberg (1993), and Hoyle (2006) among many others.

Thermal convection patterns near the onset of the Rayleigh–Bénard instability in a large domain are typically close to spatially periodic, with a characteristic horizontal length-scale given by the depth of the fluid layer. Although the preferred planform of convection depends on the precise nature of the upper and lower boundary conditions and the extent to which the fluid obeys the Boussinesq approximation, for many situations parallel stripe or ‘roll’ patterns are both theoretically predicted and experimentally observed. More recently it has become apparent that pattern forming systems may form localised structures, often referred to as ‘dissipative solitons’, rather than spatially periodic patterns. Examples of this phenomenon have been observed in vertically vibrated layers of granular media (Umbanhowar et al. 1996) (where they were named ‘oscillons’), planar gas discharge experiments (Strümpel et al. 2001), surface catalysis reactions (Rotermund et al. 1991) and thermal convection in a binary fluid. Localised states containing a number of steady convection cells in a binary fluid have been observed recently in numerical simulations by Batiste and Knobloch (2005). In parallel, there has been considerable interest in simplified model PDEs, often extensions of the Swift–Hohenberg equation, Swift & Hohenberg, 1977), that display localised solutions (Sakaguchi & Brand 1996, Hunt et al. 2000, Coulet et al. 2000).

(a)



(b)

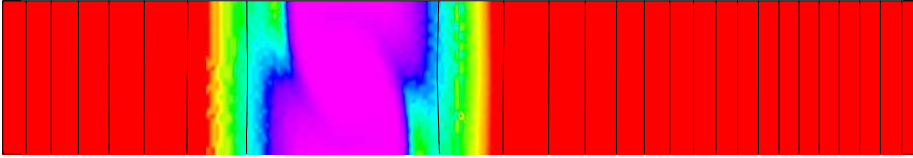


FIGURE 1. (reproduced from Blanchflower, 1999b) Numerical solution of the Boussinesq equations for thermal convection in a vertical magnetic field at $R = 100000$, $Q = 100000$, $\zeta = 0.1$, $\sigma = 1.0$. Domain aspect ratio $L = 6.0$. (a) Deviations from the background conductive temperature profile, with velocity arrows superposed. (b) Contours of magnetic field strength with superposed field lines.

Numerical simulations of two-dimensional Boussinesq magnetoconvection with an imposed vertical magnetic field, by Blanchflower (1999a,b) showed, surprisingly, that localised structures were stable for parameter values where regular arrays of convection cells of equal strengths were expected. Blanchflower referred to these localised states as ‘convectons’. Figure 1 shows a typical localised solution to the Boussinesq equations.

Convectons are closely related to the mechanism of ‘flux expulsion’ by which vigorous fluid eddies expel the magnetic field from their interior and convect more strongly as a result (Weiss 1966,1981a,1981b). This process has been observed to occur equally well in numerical simulations of compressible magnetoconvection (Hurlburt and Toomre 1988). Motivation for such numerical calculations comes from observations of small bright points (‘umbral dots’) within the dark central region (‘umbra’) of sunspots, despite the fact that the magnetic field is much stronger here than in the surrounding ‘quiet’ regions of the solar surface (Weiss 2002).

Recent theoretical work by Cox and Matthews and co-authors (2000,2001,2003,2004), in a weakly nonlinear framework, showed that a space-periodic array of identical convection cells may be destabilised by interactions with a dynamically evolving large-scale mean magnetic field and break up into localised vigorous cells separated by very weak, or no, convection. As an aside, it should be noted that the same set of weakly nonlinear amplitude equations were derived by Komarova and Newell (2000) as a model of sand banks on the ocean floor. While the analysis of Cox and Matthews provides strong support for the argument that interactions between the mean magnetic field and regular cellular convection lead to localisation, these calculations are restricted by their weakly nonlinear nature in two ways. Firstly, the ‘localised’ solutions that result are localised only on the asymptotically long length-scale of the pattern envelope. Secondly, only small deviations from a uniform strength imposed field are allowed.

In contrast, this paper attempts to describe truly localised, single cell, states and allows the large scale field to vary by an order one amount between the non-magnetic vigorously convecting eddies and the strong magnetic field convection-free regions. We take advantage of the useful observation, made by Blanchflower (1999b), that the nature of these

localised states is illuminated by a simplified system of PDEs obtained by assuming a simple sinusoidal form for their vertical structure.

The structure of the paper is as follows. In section 2 we introduce the simplified PDEs integrated numerically by Blanchflower (1999a,b) and outline a strategy for constructing solutions. In section 3 we compute approximate solutions in each of three regions using various asymptotic limits. Section 4 shows that the approximate model predicts the existence of convectons. By varying the magnetic field strength we follow the convecton branches and determine that they terminate in a saddle-node bifurcation, as conjectured by previous authors. In section 5 we show that the approximate model also describes branches of multiple-roll convectons and explains numerical observations, made by Blanchflower, of a sequence of abrupt changes in the number of convection cells. Section 6 discusses the region of the parameter space where convectons exist and presents a numerically-determined scaling law for the location of the saddle-node bifurcations. The paper closes with a discussion in section 7.

2. Governing equations

We consider an incompressible magnetically conducting fluid in the Boussinesq approximation (Chandrasekhar 1961). After the usual nondimensionalisation, the governing equations for a two dimensional flow are (see Knobloch et al. 1981 and Proctor & Weiss 1982):

$$\partial_t \omega + J[\psi, \omega] = -\sigma R \partial_x \theta - \sigma \zeta Q (J[A, \nabla^2 A] + \partial_z \nabla^2 A) + \sigma \nabla^2 \omega, \quad (2.1)$$

$$\partial_t \theta + J[\psi, \theta] = \nabla^2 \theta + \partial_x \psi, \quad (2.2)$$

$$\partial_t A + J[\psi, A] = \partial_z \psi + \zeta \nabla^2 A, \quad (2.3)$$

where the Jacobian $J[f, g] = \partial_x f \partial_z g - \partial_z f \partial_x g$. $\theta(x, z, t)$ is the temperature perturbation to the conduction profile $T = 1 - z$ and $\psi(x, z, t)$ is the streamfunction. The velocity field is given by $\mathbf{u} = \nabla \times (\psi(x, z, t) \hat{\mathbf{y}})$ and the scalar vorticity is given by $\omega = -\nabla^2 \psi$. $A(x, z, t)$ is the magnetic flux function, yielding the magnetic field

$$\mathbf{B} = \mathbf{B}_0 + \nabla \times A \hat{\mathbf{y}} = (-\partial_z A, 0, 1 + \partial_x A), \quad (2.4)$$

where $\mathbf{B}_0 = (0, 0, 1)$ is the nondimensionalised imposed uniform vertical field.

There are four dimensionless parameters: the Prandtl number $\sigma = \nu/\kappa$ (viscous / thermal diffusivity ratio); the magnetic Prandtl number $\zeta = \eta/\kappa$ (magnetic / thermal diffusivity ratio); the Chandrasekhar number Q and the Rayleigh number R :

$$R = \frac{\hat{\alpha} g \Delta T d^3}{\kappa \nu}, \quad Q = \frac{|\mathbf{B}_0|^2 d^2}{\mu_0 \rho_0 \nu \eta}. \quad (2.5)$$

The symbols $\hat{\alpha}$, g and ΔT denote, as is standard, the thermal expansion coefficient, gravitational acceleration and temperature difference between upper and lower boundaries respectively. The boundary conditions taken are the standard ones that allow an analytical treatment: fixed temperature $\theta = 0$ and a stress-free velocity field $\psi = \omega = 0$ at the upper and lower boundaries $z = 0, 1$ where the field is constrained to be vertical, i.e. $\partial_z A = 0$. Periodic boundary conditions are taken in the horizontal.

Numerical simulations and physical intuition indicate that the convecton solutions do not have a complicated z -dependence. We adopt the simplification that the z -dependence of each variable may be taken to be just the first Fourier mode that satisfies the upper and lower boundary conditions. A key part of the formation of convectons would, however, seem to be the separate evolution of a mean (i.e. z -independent) component of the

magnetic field and the leading-order z -dependent part. Therefore we follow Blanchflower and propose the minimal Fourier decomposition *ansatz*:

$$\begin{aligned}\psi &= \psi_1(x, t) \sin \pi z, \\ \omega &= \omega_1(x, t) \sin \pi z, \\ \theta &= \theta_1(x, t) \sin \pi z + \theta_2(x, t) \sin 2\pi z, \\ A &= A_0(x, t) + A_1(x, t) \cos \pi z.\end{aligned}$$

Such a decomposition was first considered by Knobloch et al. (1981). We substitute these expressions into (2.1) - (2.3) and neglect higher order Fourier modes. The inclusion of $\theta_2(x, t)$ provides the leading-order nonlinearity near the onset of convection in the hydrodynamic Rayleigh–Bénard problem, as in the derivation of the ‘Lorenz equations’ (Lorenz 1963). The truncation results in the following set of PDEs that will be the focus of the rest of this paper:

$$\partial_t \omega_1 = \sigma(\omega_1'' - \pi^2 \omega_1) - \sigma R \theta_1' - \sigma \zeta Q \pi [(1 + A_0')(\pi^2 A_1 - A_1'') + A_0''' A_1], \quad (2.6)$$

$$\partial_t \theta_1 = \theta_1'' - \pi^2 \theta_1 + \psi_1'(1 + \pi \theta_2) + \frac{\pi}{2} \psi_1 \theta_2', \quad (2.7)$$

$$\partial_t \theta_2 = \theta_2'' - 4\pi^2 \theta_2 + \frac{\pi}{2} (\psi_1 \theta_1' - \psi_1' \theta_1), \quad (2.8)$$

$$\partial_t A_0 = \zeta A_0'' + \frac{\pi}{2} (\psi_1 A_1)', \quad (2.9)$$

$$\partial_t A_1 = \zeta (A_1'' - \pi^2 A_1) + \pi \psi_1 (1 + A_0'), \quad (2.10)$$

where primes denote ∂_x , and $\omega_1 = \pi^2 \psi_1 - \psi_1''$. An illustrative convecton solution to (2.6) - (2.10) is shown in figure 2. The construction of approximate steady solutions proceeds by dividing up the spatial domain into three regions: inside the convecton, where the field is expelled and the flow is vigorous, a thin magnetic boundary layer where the flow becomes very weak and the field reaches a peak intensity, and an outside region containing a much wider thermal ‘boundary layer’ where the flow is negligible but the field is still distorted. In this thermal boundary layer the dominant balance is between the temperature gradient and the Lorentz force terms in the momentum equation. These impart equal and opposite vorticity to the flow which allows the fluid to remain stationary. The three regions can be easily distinguished in figure 2. Numerical simulations indicate that the mean magnetic field is completely expelled from the inside region: consequently $A_0' = -1$ within the convecton.

We make three general remarks about (2.6) - (2.10). Firstly, numerical results indicate that in the outside region, to a very high degree of accuracy,

$$A_0' = \frac{l_c}{L - l_c}, \quad (2.11)$$

for a domain of length L and a convecton of width l_c (as measured by the distance between the discontinuities in A_0'). This is due to the imposition of periodic boundary conditions, and the fact that $|\psi_1| \ll 1$ in the outside region. Secondly, the rescaling $A_1 = \zeta \hat{A}_1$ removes odd powers of ζ , showing that a small- ζ expansion (which we will employ to describe the ‘inside’ region) should proceed by expanding in powers of ζ^2 . Thirdly, (2.9) may be integrated directly. This, using (2.11) to determine the constant of integration, yields

$$\psi_1 A_1 = \frac{2\zeta}{\pi} \left(\frac{l_c}{L - l_c} - A_0' \right). \quad (2.12)$$

Finally, we define the geometric parameter $\beta = (L - l_c)/L$. An expression that will occur

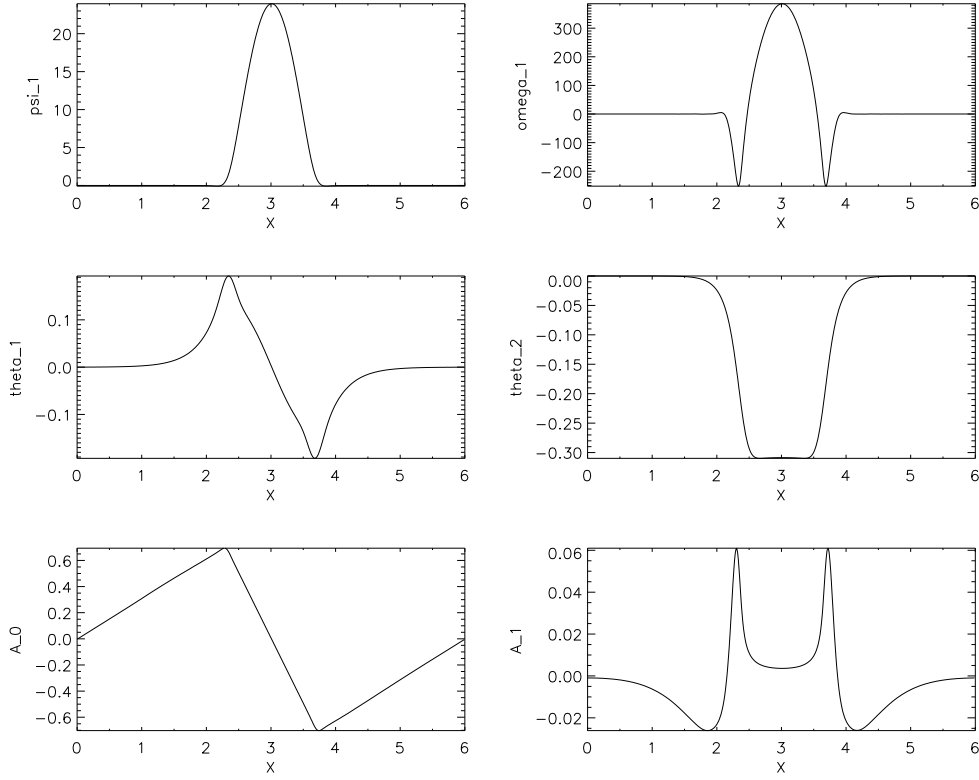


FIGURE 2. Numerical solution to the truncated equations (2.6) - (2.10) for $R = 20000$, $Q = 14000$, $\zeta = 0.1$, $\sigma = 1.0$, $L = 6.0$.

repeatedly is the leading-order value of $1 + A'_0$ in the outside region: this is $1 + l_c / (L - l_c) = 1/\beta$.

3. Approximate solutions

In this section we discuss approximate solutions of the model system (2.6) - (2.10) that reflect the physics of the system in the three regions described above. The approximate solutions for $A_1(x)$ are then patched together; the conditions for patching determine whether convection solutions are possible for a given combination of parameters.

3.1. The inside region

For the inside region we develop an asymptotic expansion in powers of $\zeta \ll 1$. Since the large scale magnetic field is negligible in this region we set $A'_0 = -1$ at leading order. As a result (2.6) is linear at leading order and the hydrodynamics is decoupled from the magnetic field. Formally we expand as follows:

$$\begin{aligned}
 (\psi_1, \omega_1) &= (\psi_{10}, \omega_{10}) + \zeta^2(\psi_{11}, \omega_{11}) + O(\zeta^4), \\
 (\theta_1, \theta_2) &= (\theta_{10}, \theta_{20}) + \zeta^2(\theta_{11}, \theta_{21}) + O(\zeta^4), \\
 A_1 &= \zeta A_{10} + \zeta^3 A_{11} + O(\zeta^5), \\
 A'_0 &= -1 + \zeta^2 A'_{01} + O(\zeta^4),
 \end{aligned}$$

and take $\psi_{10} = \hat{\psi}_0 \sin kx$ where $\hat{\psi}_0$ is a constant. We fix the origin $x = 0$ to be at the left-hand edge of the convection cell (at $x = 2.5$ in figure 2). Then $\omega_{10} = \hat{\beta}^2 \hat{\psi}_0 \sin kx$ where $\hat{\beta}^2 = \pi^2 + k^2$, and

$$\theta_{10} = \frac{\hat{\beta}^4 \hat{\psi}_0}{Rk} \cos kx. \quad (3.1)$$

From the temperature equations (2.7) and (2.8) we have

$$0 = - \left(\frac{\hat{\beta}^6 \hat{\psi}_0}{Rk} - k\hat{\psi}_0 \right) \cos kx + \pi k \hat{\psi}_0 \theta_{20} \cos kx + \frac{\pi \hat{\psi}_0}{2} \theta'_{20} \sin kx, \quad (3.2)$$

$$0 = \theta''_{20} - 4\pi^2 \theta_{20} - \frac{\pi \hat{\beta}^4 \hat{\psi}_0^2}{2R},$$

which have the obvious solution $\theta_{20} = -\hat{\beta}^4 \hat{\psi}_0^2 / (8\pi R)$, constant. Numerical simulations such as figure 2 show that θ_2 attains a constant value across convectons that are sufficiently wide. As θ_{20} is constant, (3.2) implies

$$\hat{\psi}_0^2 = \frac{8}{\hat{\beta}^4} \left(R - \frac{\hat{\beta}^6}{k^2} \right). \quad (3.3)$$

Finally, from (2.12) we find $\psi_{10} A_{10} = 2/(\pi\beta)$ and hence

$$A_1 = \frac{2\zeta}{\pi\beta\hat{\psi}_0} \operatorname{cosec} kx + O(\zeta^3). \quad (3.4)$$

The hydrodynamic equations at $O(\zeta^2)$ are formidably complicated. Further useful information can be extracted from (2.10) at $O(\zeta^2)$ and from (2.12) at $O(\zeta^3)$; from (2.10) we obtain

$$0 = A''_{10} - \pi^2 A_{10} + \pi \psi_{10} A'_{01},$$

which can be solved for A'_{01} . Hence

$$A'_0 = -1 + \frac{2\zeta^2}{\pi^2 \beta \hat{\psi}_0^2} \left(\frac{\hat{\beta}^2}{\sin^2 kx} - \frac{2k^2}{\sin^4 kx} \right) + O(\zeta^4). \quad (3.5)$$

This expression indicates that the expansion in powers of ζ breaks asymptoticity when $x = O(\zeta^{1/2})$; at this point the second term in the $O(\zeta^2)$ contribution becomes $O(1)$.

Now we turn to the terms in (2.12) at $O(\zeta^3)$:

$$\psi_{11} A_{10} + \psi_{10} A_{11} = -\frac{2}{\pi} A'_{01}. \quad (3.6)$$

where both ψ_{11} and A_{11} are unknown. The later analysis is found to be greatly improved if the term A_{11} is included in the solution for A_1 . Given the difficulties in obtaining analytically anything more than the leading order terms for ψ_1 , θ_1 and θ_2 , we elect to neglect the term ψ_{11} and solve (3.6) for A_{11} :

$$A_{11} = -\frac{2A'_{01}}{\pi\psi_{10}} = -\frac{4}{\pi^3 \beta \hat{\psi}_0^3} \left(\frac{\hat{\beta}^2}{\sin^3 kx} - \frac{2k^2}{\sin^5 kx} \right).$$

The inside solution (3.4) for A_1 is then

$$A_1 = \frac{2\zeta}{\pi\beta\hat{\psi}_0} \operatorname{cosec} kx + \frac{4\zeta^3}{\pi^3 \beta \hat{\psi}_0^3} \left(\frac{2k^2}{\sin^5 kx} - \frac{\hat{\beta}^2}{\sin^3 kx} \right) + O(\zeta^5). \quad (3.7)$$

When $x = O(\zeta^{1/2})$ we see that *both* terms in (3.7) are $O(\zeta^{1/2})$, breaking asymptoticity at the same point as (3.5) does; this illustrates the importance of A_{11} . We remark that a similar approach involving taking a very simple solution for the hydrodynamic part of the problem, but solving in detail for the magnetic field structure, was used by Busse (1975) in the analysis of spatially periodic convection cells.

The required rescalings to continue the asymptotics when $x = O(\zeta^{1/2})$ can be computed in a straightforward manner, but it appears that nothing can be easily deduced from the rescaled ODEs.

3.2. The outside region

3.2.1. The limit $\zeta \ll 1$

The outside region contains the thermal boundary layer and a balance between buoyancy and Lorentz forces in the momentum equation. A natural assumption would be that $|\psi_1| \ll 1$ and the leading-order balance in the momentum equation (2.6) is

$$-R\theta_1' \approx \frac{\zeta Q \pi}{\beta} (\pi^2 A_1 - A_1''), \quad (3.8)$$

(recall that, at leading order, $1 + A_0' = 1/\beta$, constant). However there is no consistent scaling in powers of ζ that removes the $\omega'' - \pi^2 \omega$ terms to higher orders in the momentum equation, while maintaining the leading-order balance (3.8). This can be seen by the following argument. Firstly, we demand $\theta_1 = O(\zeta^0)$ since the solution for θ_1 in the inside region (3.1) is purely hydrodynamic, and hence independent of ζ , at leading order. Then from (3.8) we observe that $A_1 = O(\zeta^{-1})$. (2.10) then implies

$$\zeta(\pi^2 A_1 - A_1'') = \frac{\pi}{\beta} \psi_1,$$

and so $\psi_1 = O(\zeta^0)$. Then (2.12) indicates that

$$\psi_1 A_1 = \zeta \left(\frac{l_c}{L - l_c} - A_0' \right) = O(\zeta^{-1}), \quad (3.9)$$

and so the ‘small correction’ to the leading-order approximation $A_0' = l_c/(L - l_c)$ is in fact $O(\zeta^{-2})$! Hence it is not possible, asymptotically in the limit $\zeta \rightarrow 0$, to describe a solution of the form we require for the outside region. It is impossible for the magnetic field to distort and provide the required Lorentz force to balance the temperature gradient in this limit.

3.2.2. The limit $R \gg 1$, $Q = O(R)$

A consistent leading-order description can, however, be captured in the limit $R \gg 1$, keeping $Q = O(R)$. This is less satisfactory than the small- ζ limit, since it is clear from numerical results that R and Q do not have to be particularly large for convectons to exist. We adopt the rescaling

$$(\omega_1, \psi_1, \theta_1, \theta_2, A_1) = R^{-1}(\tilde{\omega}_1, \tilde{\psi}_1, \tilde{\theta}_1, \tilde{\theta}_2, \tilde{A}_1),$$

and assume that $Q = O(R)$ and $A_0' = O(1)$. This yields (dropping the tildes)

$$0 = -\theta_1' - \frac{\pi \zeta Q}{R} [(1 + A_0')(\pi^2 A_1 - A_1'') + A_0''' A_1] + \frac{1}{R}(\omega_1'' - \pi^2 \omega_1), \quad (3.10)$$

$$0 = \frac{1}{R}(\theta_1'' - \pi^2 \theta_1 + \psi_1') + \frac{1}{R^2} \left(\pi \psi_1' \theta_2 + \frac{\pi}{2} \psi_1 \theta_2' \right), \quad (3.11)$$

$$0 = \frac{1}{R}(\theta_2'' - 4\pi^2 \theta_2) + \frac{\pi}{2R^2}(\psi_1 \theta_1' - \psi_1' \theta_1), \quad (3.12)$$

$$\frac{1}{R^2}\psi_1 A_1 = \frac{2\zeta}{\pi} \left(\frac{l_c}{L-l_c} - A'_0 \right), \quad (3.13)$$

$$0 = \zeta(A''_1 - \pi^2 A_1) + \pi\psi_1(1 + A'_0). \quad (3.14)$$

We expand in powers of R^{-1} :

$$\begin{aligned} (\psi_1, \theta_1, A_1) &= (\psi_{10}, \theta_{10}, A_{10}) + R^{-1}(\psi_{11}, \theta_{11}, A_{11}) + O(R^{-2}), \\ A'_0 &= \frac{l_c}{L-l_c} + R^{-2}A'_{02} + O(R^{-2}), \end{aligned}$$

and consider the leading order terms in (3.10), (3.11) and (3.14):

$$0 = -\theta'_{10} - \frac{\pi\zeta Q}{\beta R}(\pi^2 A_{10} - A''_{10}), \quad (3.15)$$

$$0 = \zeta(A''_{10} - \pi^2 A_{10}) + \frac{\pi}{\beta}\psi_{10}, \quad (3.16)$$

$$0 = \theta''_{10} - \pi^2 \theta_{10} + \psi'_{10}. \quad (3.17)$$

Selecting the solution that decays as $x \rightarrow -\infty$ and introducing

$$h = \sqrt{\frac{\pi^4 Q}{\pi^2 Q - \beta^2 R}}, \quad (3.18)$$

we obtain the leading order solution

$$\psi_1 = -\frac{\beta^2 h R \hat{\phi}_0}{\pi^2 Q} e^{hx} + O(R^{-1}), \quad (3.19)$$

$$\theta_1 = \hat{\phi}_0 e^{hx} + O(R^{-1}), \quad (3.20)$$

$$A_1 = \frac{\beta h R \hat{\phi}_0}{\pi \zeta Q (h^2 - \pi^2)} e^{hx} + \hat{\phi}_1 e^{\pi x} + O(R^{-1}). \quad (3.21)$$

From inspecting (3.13) we observe that the assumption $R^2 \zeta \gg 1$ is necessary in addition to our previous assumptions that $R \gg 1$ and $\zeta \ll 1$. This additional assumption is necessary mathematically but forms no restriction in practice, as typical numerical values are $R \approx 10^4$ and $\zeta \approx 10^{-1}$.

3.3. The boundary layer

The boundary layer near $x = 0$ (the left hand edge of the convection cell) smooths the transition between the inside region where $A'_0 = -1$, and the outside region where $1 + A'_0$ takes the constant non-zero value $1/\beta$. As figure 2 illustrates, the change in the gradient of A_0 is sharp even for $\zeta = 0.1$. A simple functional form for $A_0(x)$ within the boundary layer is proposed: the hyperbola

$$\left(A_0 - \frac{l_c x}{L - l_c} \right) (A_0 + x) = \varepsilon, \quad (3.22)$$

where ε is a small parameter that determines the spatial extent of the magnetic boundary layer. Such a simple functional form allows analytical progress to be made on the form of $A_1(x)$. Substituting for ψ_1 by using (2.12) in (2.10) we obtain

$$A_1(\pi^2 A_1 - A''_1) = 2(1 + A'_0) \left(\frac{l_c}{L - l_c} - A'_0 \right),$$

which becomes, after substituting for A'_0 using (3.22):

$$A_1(\pi^2 A_1 - A''_1) = \frac{2\varepsilon}{x^2 + 4\varepsilon\beta^2}. \quad (3.23)$$

Clearly there are two relevant scalings. There is an ‘outer’ scaling where $x \gg \varepsilon^{1/2}$ and an ‘inner’ scaling where $x = O(\varepsilon^{1/2})$. The outer scaling is of little interest here, since we expect (3.23) to be valid only near $x = 0$. To examine the inner scaling we introduce a rescaled variable X defined by $x = 2\beta\varepsilon^{1/2}X$. Now (3.23) becomes

$$4\varepsilon\beta^2\pi^2 A_1^2 - A_1 A''_1 = \frac{2\varepsilon}{X^2 + 1}, \quad (3.24)$$

where primes now denote ∂_X . We seek a solution in powers of ε that is even about $X = 0$, starting with an $O(\varepsilon^0)$ term since the outside solution, to which we need to match, has an $O(1)$ variation in A_1 caused by the horizontal variation in temperature in the thermal boundary layer. Let

$$A_1 = A_{10} + \varepsilon A_{11} + O(\varepsilon^2).$$

At leading order we obtain

$$-A_{10}A''_{10} = 0, \quad (3.25)$$

and set $A_{10} = \alpha_0$ constant. A_{10} contains no linear term because of the symmetry of (3.24). At $O(\varepsilon)$ we obtain

$$4\beta^2\pi^2\alpha_0^2 - \alpha_0 A''_{11} = \frac{2}{X^2 + 1},$$

which has the solution

$$A_{11} = 2\pi^2\beta^2\alpha_0 X^2 - \frac{2X}{\alpha_0} \tan^{-1} X + \frac{1}{\alpha_0} \log(1 + X^2).$$

In terms of the original variable x :

$$A_{1,bl} = \alpha_0 + \frac{\pi^2}{2}\alpha_0 x^2 - \frac{\varepsilon^{1/2}x}{\alpha_0\beta} \tan^{-1} \left(\frac{x}{2\beta\varepsilon^{1/2}} \right) + \frac{\varepsilon}{\alpha_0} \log \left(1 + \frac{x^2}{4\beta^2\varepsilon} \right).$$

where the subscript *bl* indicates ‘boundary layer’.

3.4. Patching conditions

The approximate solution contains five undetermined coefficients. These are $\hat{\phi}_0, \hat{\phi}_1$ (in the outside region), ε, α_0 (in the boundary layer) and k (in the inside region). The parameters R, Q, ζ and L are treated as given. The convection width is given by $l_c = \pi/k$, and we specify the centre of the left-hand boundary layer between inside and outside solutions to be $x = 0$. By the symmetry of the convection there is no need to consider patching near the right-hand boundary layer at $x = l_c$.

Our five patching conditions are as follows. We patch the outside solution for A_1 to the boundary layer solution at a point $x = -p < 0$, demanding that A_1 and A'_1 are continuous. Similarly we patch the boundary layer solution to the inside solution for A_1 at $x = p > 0$. Note that, by the symmetry of the boundary layer solution, $A'_{1,bl}(p) = -A'_{1,bl}(-p)$ and the inside and outside solutions are directly related to each other. The fifth condition is that the temperature perturbation θ_1 attains equal values at $x = \pm p$; the temperature perturbation that drives the perturbation to A_1 in the outside region is given by the temperature perturbation excited by the strength of the convection within the inside region. In total we have five natural patching conditions and

six unknowns: the patching location p and the five undetermined coefficients. The lack of an imposed scaling relationship between ε and ζ accommodates the approximations made in the solutions derived in each region. The patching requirements are expressed in the following equations.

$$\alpha_0 \left(1 + \frac{\pi^2 p^2}{2} \right) - \frac{\varepsilon^{1/2} p}{\alpha_0 \beta} \tan^{-1} \left(\frac{p}{2\varepsilon^{1/2} \beta} \right) + \frac{\varepsilon}{\alpha_0} \log \left(1 + \frac{p^2}{4\varepsilon \beta^2} \right) = \frac{\beta h R \hat{\phi}_0}{\pi \zeta Q (h^2 - \pi^2)} e^{-hp} + \hat{\phi}_1 e^{-\pi p}, \quad (3.26)$$

$$-\pi^2 \alpha_0 p + \frac{\varepsilon^{1/2}}{\alpha_0 \beta} \tan^{-1} \left(\frac{p}{2\varepsilon^{1/2} \beta} \right) = \frac{\beta h^2 R \hat{\phi}_0}{\pi \zeta Q (h^2 - \pi^2)} e^{-hp} + \pi \hat{\phi}_1 e^{-\pi p}, \quad (3.27)$$

$$\hat{\phi}_0 e^{-hp} = \frac{\hat{\beta}^4 \hat{\psi}_0}{Rk} \cos kp, \quad (3.28)$$

$$\begin{aligned} \alpha_0 \left(1 + \frac{\pi^2 p^2}{2} \right) - \frac{\varepsilon^{1/2} p}{\alpha_0 \beta} \tan^{-1} \left(\frac{p}{2\beta \varepsilon^{1/2}} \right) + \frac{\varepsilon}{\alpha_0} \log \left(1 + \frac{p^2}{4\varepsilon \beta^2} \right) \\ = \frac{2\zeta}{\pi \beta \hat{\psi}_0} \operatorname{cosec} kp + \frac{4\zeta^3}{\pi^3 \beta \hat{\psi}_0^3} \left(\frac{2k^2}{\sin^5 kp} - \frac{\hat{\beta}^2}{\sin^3 kp} \right), \end{aligned} \quad (3.29)$$

$$\begin{aligned} \pi^2 \alpha_0 p - \frac{\varepsilon^{1/2}}{\alpha_0 \beta} \tan^{-1} \left(\frac{p}{2\beta \varepsilon^{1/2}} \right) = -\frac{2\zeta k \cos kp}{\pi \beta \hat{\psi}_0 \sin^2 kp} \\ - \frac{4k\zeta^3}{\pi^3 \beta \hat{\psi}_0^3} \left(\frac{10k^2 \cos kp}{\sin^6 kp} - \frac{3\hat{\beta}^2 \cos kp}{\sin^4 kp} \right). \end{aligned} \quad (3.30)$$

We recall that $\hat{\psi}_0^2 = 8(R - \hat{\beta}^6/k^2)/\hat{\beta}^4$, $\hat{\beta}^2 = k^2 + \pi^2$, $\beta = (L - l_c)/L$ and $l_c = \pi/k$. We fix $p = 0.1$: the qualitative nature of the solutions is not affected by this choice.

4. Results for single roll convectons

4.1. Solutions of the patching conditions

In this section we look for numerical solutions of the patching conditions (3.26) - (3.30) and compare them with solutions of the PDEs (2.6) - (2.10).

We fix parameter values at $R = 20000$, $\zeta = 0.1$, $\sigma = 1.0$ and $L = 6.0$ and consider $Q = 14000$ and $Q = 35000$. Perhaps surprisingly, for both of these values of Q there exist two solutions to the patching conditions; these correspond to convectons of different widths l_c , see table 1.

Figures 3 and 4 compare the two solutions of the patching conditions at $Q = 14000$ with the numerical solution of (2.6) - (2.10). The wider approximate solution is a much better fit; although the value of l_c is substantially too high, it gives excellent agreement with the height and width of the local maximum of A_1 in the boundary layer.

Figure 5 illustrates the approximate solutions for wide and narrow convectons at $Q = 35000$. We observe that they are now much more similar in form, and this suggests that they may collide and disappear in a saddle-node bifurcation as Q is increased further.

Q		ε	$\hat{\phi}_0$	$\hat{\phi}_1$	k	α_0	$l_c = \pi/k$
14000	wide (stable)	7.481×10^{-5}	0.2603	-4.6213	1.1445	0.06038	2.7449
14000	narrow (unstable)	1.715×10^{-4}	0.1193	-1.1099	9.3421	0.05397	0.3363
35000	wide (stable)	4.546×10^{-6}	0.1634	-1.9261	2.8958	0.02581	1.0849
35000	narrow (unstable)	1.046×10^{-5}	0.1619	-1.6919	6.1116	0.03006	0.5140

TABLE 1. Patching coefficients for wide and narrow convectons at $Q = 14000$ and $Q = 35000$. Other parameters are: $R = 20000$, $\zeta = 0.1$, $\sigma = 1.0$, $L = 6.0$, $p = 0.1$.

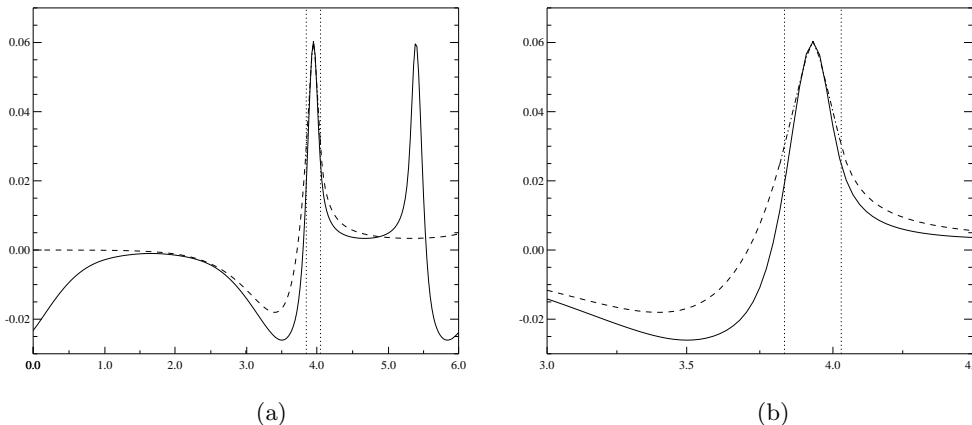


FIGURE 3. Comparison between numerical solution for A_1 (solid line) from (2.6) - (2.10), as shown in figure 2, and the approximate solution using the coefficients in the first line of table 1. $R = 20000$, $Q = 14000$, $\zeta = p = 0.1$, $L = 6.0$. The left-side and right-side dashed lines are the outside and inside solutions respectively. The boundary layer solution is shown dot-dashed. The right-hand boundary layer and outside solution are not shown due to the extreme width of the model solution, but these are symmetrically related to those shown. Vertical dotted lines indicate the patching points. (b) is an enlargement of (a).

4.2. Validity and stability of approximate solutions

Various assumptions implicit in the construction of the approximate solutions mean that not all possible solutions to the patching conditions correspond to convectons.

Without loss of generality, since (2.6) - (2.10) are symmetric under the operation $(\psi_1, \omega_1, \theta_1, A_1) \rightarrow -(\psi_1, \omega_1, \theta_1, A_1)$, we may fix $\alpha_0 > 0$ so that $A_1 > 0$ in the boundary layer and the convection roll circulates clockwise. So we expect $\hat{\phi}_0 > 0$ by (3.1), since the temperature perturbation $\theta_1 > 0$ at $x = 0$, and $\hat{\phi}_1 < 0$ because we require A_1 to cross through zero at some point, see (3.21). These conditions are all clearly satisfied by the solutions found in table 1 above.

Further restrictions on the validity of the approximate solutions are, firstly, that we require the amplitude $\hat{\psi}_0^2$ to be positive; (3.3) shows that for a fixed R there is a finite range of acceptable wavenumbers k . For $R = 20000$, $\hat{\psi}_0^2 > 0$ gives

$$0.22 < k < 11.24. \quad (4.1)$$

Secondly, we require the boundary layer to be small compared to the width of the convecton: $\varepsilon \ll 1$. Thirdly, we ignore solutions of the patching conditions where the computed width of the convecton implies that it occupies such a large proportion of the domain

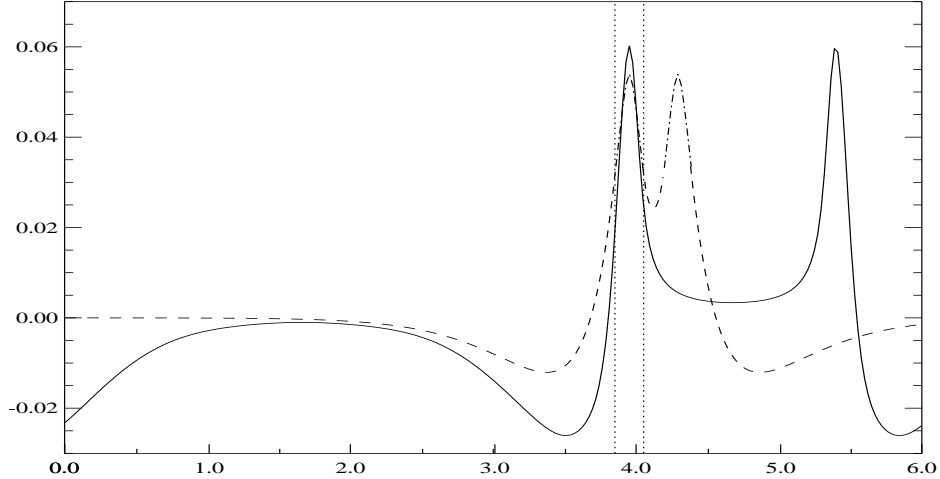


FIGURE 4. The approximate solution (dashed curve) for a narrow convecton at the same parameter values as figure 3: $R = 20000$, $Q = 14000$, $\zeta = p = 0.1$, $L = 6.0$. For comparison, the solid line (the numerical solution for the *wide* convecton at the same parameter values) from figure 3 is also shown. The right-hand boundary layer and outside solution are related by a reflection symmetry in the line $x = 4.7$ to the left-hand part of the solution, since the behaviour of A_1 is the same in both boundary layers. Vertical dotted lines indicate the patching points.

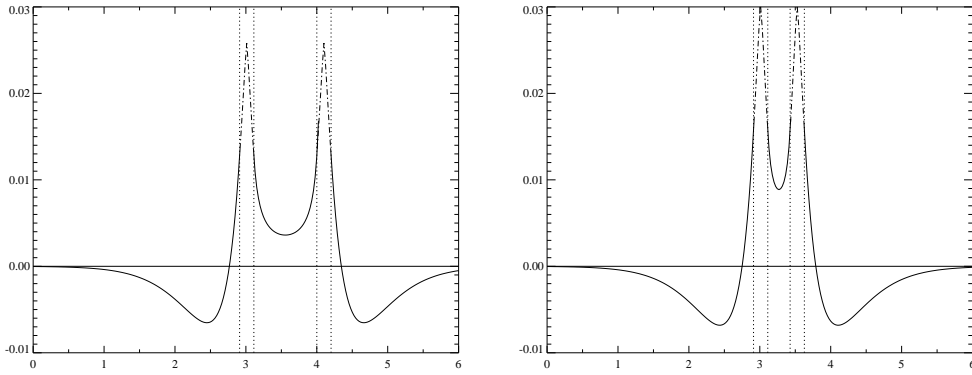


FIGURE 5. Approximate solutions for $A_1(x)$ at $Q = 35000$: (a) wide convecton; (b) narrow convecton. Other parameters are as for figure 4. Vertical dotted lines indicate the patching points between outside (solid), boundary layer (dot-dashed) and inside (solid) solutions as appropriate.

that insufficient space remains in the outside region for the outside solution to decay exponentially to small values. Since the thermal boundary layer decays as $e^{\pi x}$, we consider that a model solution will only be valid if

$$l_c < L - 2. \quad (4.2)$$

In order for a convecton solution to be dynamically stable and truly localised we require that the outside region is linearly stable to the onset of convection. Using (2.11) and (2.4) we observe that in the outside region the magnetic field has an effective strength given by $Q_{\text{eff}} = Q/\beta^2$. For fixed values of R , σ and ζ we compute the minimum value of Q that corresponds to stability for both steady and oscillatory perturbations. The linear stability

calculation for the onset of convection in a uniform vertical magnetic field, see Proctor and Weiss (1982), is usually presented as yielding the maximum Rayleigh number R for which the quiescent state is stable, at fixed Q :

$$R = \frac{\hat{\beta}^6}{k^2} c_1 + \frac{Q\pi^2 \hat{\beta}^2}{k^2} c_2, \quad (4.3)$$

where $c_1 = c_2 = 1$ for the onset of steady convection and

$$c_1 = \frac{(\sigma + \zeta)(1 + \zeta)}{\sigma}, \quad c_2 = \frac{(\sigma + \zeta)\zeta}{1 + \sigma},$$

for the onset of oscillatory convection. Rearranging (4.3) to solve for Q as a function of R , it is straightforward to locate the minimum value of Q as a function of k^2 . The result is

$$Q_{\min} = \frac{(K - \pi^2)R - K^3 c_1}{\pi^2 c_2 K},$$

$$k_{\min}^2 = K - \pi^2,$$

where $K = (R\pi^2/2c_1)^{1/3}$. The outside region is linearly stable when

$$Q > \beta^2 Q_{\min,s}, \quad \text{and} \quad Q > \beta^2 Q_{\min,o}, \quad (4.4)$$

where the subscripts s and o refer to steady and oscillatory convection respectively. The extent to which these various constraints impinge on the results is shown in figures 6 and 7.

4.3. Branches of single-roll convectons

In this section we trace the behaviour of the solutions to the patching conditions (3.26) - (3.30), as Q is varied, at fixed ζ , R and L . We find that convecton solutions cease to exist when Q exceeds a critical value, corresponding to a saddle-node bifurcation where the ‘wide’ and ‘narrow’ solution branches collide.

The continuation and bifurcation package AUTO97 (Doedel et. al. 1997) is used to follow solutions to the patching conditions; from a bifurcation-theoretic viewpoint, only steady-state bifurcations are relevant since they create or destroy branches of equilibria. Figure 6 shows the existence of a saddle-node bifurcation at approximately $Q/R = 1.9$ for the typical parameter values used above. This justifies the saddle-node bifurcation proposed by Blanchflower (1999a), his figure 3. The patching conditions do not indicate the existence of any other steady-state bifurcations.

Moreover, Blanchflower (1999a), section 3, remarks that the single-roll convecton branch (as well as solutions found for multiple convection rolls) lose their isolated nature at small Q when weak oscillatory convection sets in in the quiescent ‘outside’ region. Figure 6 supports this statement since for these parameter values the marginal stability threshold for oscillatory disturbances is much closer to the branch of approximate solutions than the stability threshold for steady-state instability.

The location of the saddle-node bifurcation ($Q = 41530$, $l_c = 0.657$) is within a factor of 2 of that determined numerically by Blanchflower: $Q = 26500$, $l_c = 0.65$, despite the gross simplifications involved. The results of section 6 show that his determination of the location of the saddle-node bifurcation is accurate only to within about 10%. Even so, it is clear that the approximate model predicts substantially wider convectons than occur in the truncated PDEs (2.6) - (2.10), becoming unrealistically wide at lower values of Q . Approximating the patching conditions in the limits $|k\zeta| \ll 1$ and $R, Q \gg 1$ leads to the

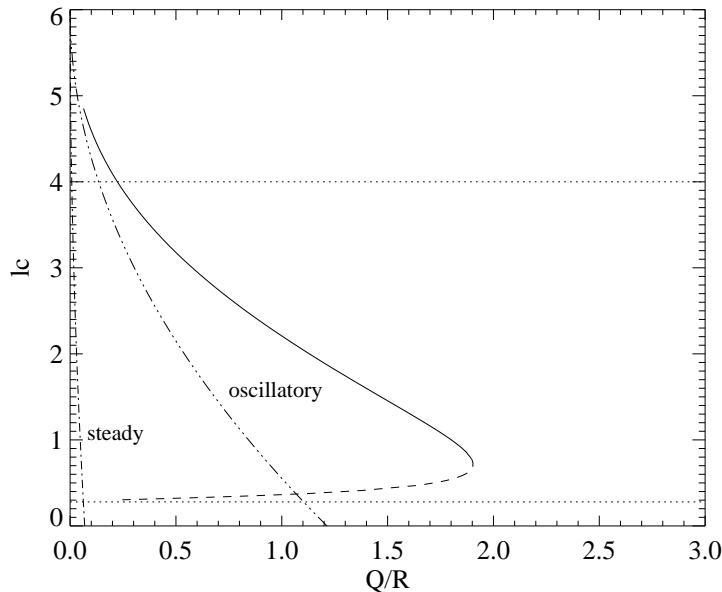


FIGURE 6. Bifurcation diagram for solutions of the patching conditions showing the approximate location of convectons in the $(Q/R, l_c)$ plane for $R = 20000$, $\zeta = 0.1$ and $L = 6.0$. Horizontal dotted lines indicate the validity limits $l_c < L - 2$ and (4.1). The dash-dotted curves give the stability criteria (4.4): convectons are stable above and to the right of these curves. The two convectons shown in figure 5 correspond to points at $Q/R = 1.75$.

result

$$\frac{Q}{R} = \frac{2}{1 - \pi\zeta} \beta^2 \equiv \frac{2}{1 - \pi\zeta} \left(1 - \frac{l_c}{L}\right)^2, \quad (4.5)$$

showing that the predicted convecton width l_c tends to the domain width L as Q/R becomes small. To counteract this systematic defect in the model we take a larger domain size L : this allows the formation of multiple-roll convectons in the approximate model.

5. Multiple-roll convectons

In this section we discuss the existence in the approximate model of states corresponding to $n > 1$ separately localised identical convection cells in a large domain. Assuming that the cells are well separated from each other, their only mutual influence is via the increase in the effective field strength caused by the expulsion of the field into the quiescent regions between each pair of cells. For each cell the effective field strength in the outside region is now $Q_{\text{eff}} = QL^2/(L - nl_c)^2$ since the field is now confined to a region of width $L - nl_c$. In the patching equations (3.26) - (3.30) we redefine $\beta = 1 - nl_c/L$. Figure 7 shows numerical computations of branches of multiple-convecton solutions for $n = 1, 2, 3, 4$. These solutions of the approximate model indicate two further points: firstly that, as Q is decreased, branches terminate where the boundary layer coordinate ε is no longer small (indicating a bifurcation in the PDEs that the model is unable to describe fully), and secondly that at very small Q/R the equations are insensitive to the exact number of convection cells; the relevant parameter is their total width.

Figure 7 indicates that the individual rolls in the stable $n = 2$ state are narrower than the single roll in the $n = 1$ state. In addition, the saddle-node bifurcation on the

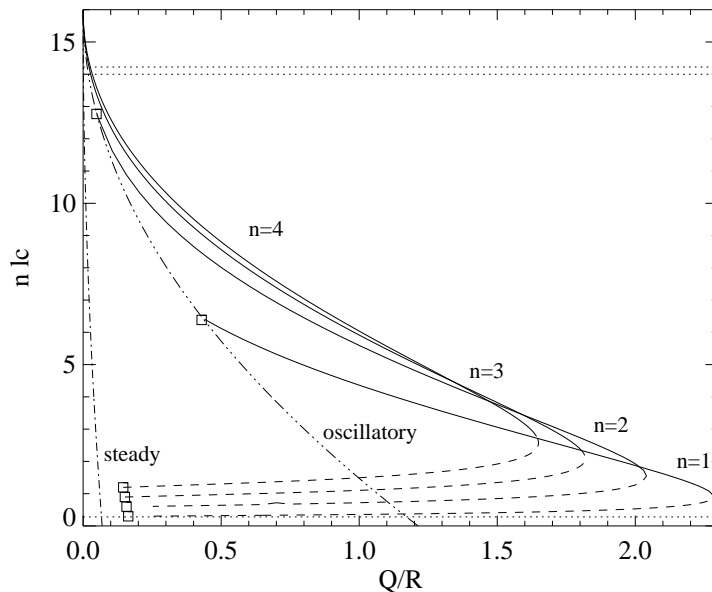


FIGURE 7. Bifurcation diagram for $R = 20000$, $\zeta = 0.1$, $\sigma = 1.0$ and $L = 16.0$. Branches of convectons from the approximate model are shown by the solid (stable) and dashed (unstable) curves. Note that the vertical axis gives the total width of the convecting region; individual cells become narrower as their number increases. The horizontal dotted and curved dash-dotted lines indicate the stability boundaries for the convection and are reproduced from figure 6. \square indicates points where the boundary-layer solution blows up ($\varepsilon \rightarrow \infty$).

$n = 2$ branch occurs at lower Q than that on the $n = 1$ branch. In a series of numerical integrations of the PDEs at increasing values of Q we therefore expect a sudden jump onto the single-roll branch at the point of the $n = 2$ saddle-node, accompanied by a widening of the convection cell, and this is observed in figure 8. The overall width of the convecting (light-coloured) region in figure 8 can be compared with the envelope of the branches in figure 7; the sharp transitions in figure 8 correspond to approaching a saddle-node bifurcation and then ‘falling’ onto a new solution branch with a lower number of convection cells. Figure 8 was constructed by increasing Q in small increments; numerical simulations conducted by decreasing Q , starting from the single-roll convecton state would obtain a very different picture: we predict that the single-roll state persists to lower Q and then either bifurcates to a larger number of rolls (when the single roll can no longer be sustained) or is replaced by weak convection throughout the layer (when the linear stability boundary for the outside region is crossed).

The $n = 1$ branch in figure 7 terminates at approximately $Q/R = 0.45$; at this point the boundary layer width ε diverges to infinity and the solution to the approximate model cannot be continued. This behaviour is unrelated to the proximity of the dash-dotted curve giving the linear stability of the outside region to oscillatory disturbances. The latter varies with σ and the former does not, since σ does not enter into the patching conditions. This indicates that as Q decreases there are two possible mechanisms for instability of convectons: boundary-layer blow-up and outer region (oscillatory) instability. We return to this point in section 6.

Note that the $n = 2$ branch also undergoes boundary-layer blow-up, but at $Q/R \approx 0.05$. For small Q/R we remark that the width of the domain filled with convecting cells is

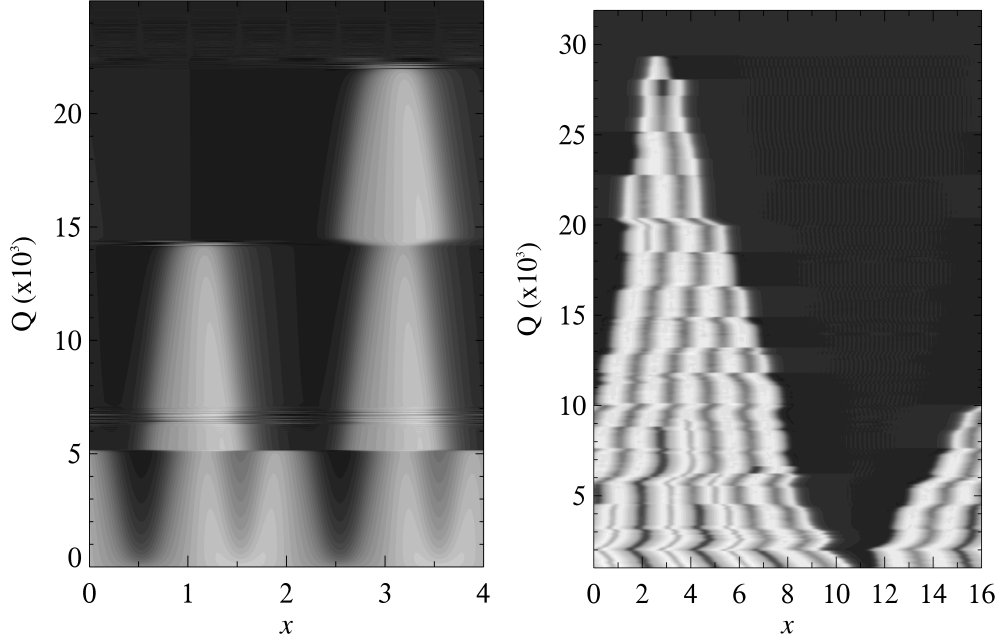


FIGURE 8. (reproduced from Blanchflower, 1999b) Numerical integrations of (2.6) - (2.10): contour plots of dT/dz at the upper boundary of the layer $z = 1$, after transients have decayed. Light colours correspond to convection cells, dark to quiescent fluid. $R = 20000$, $\zeta = 0.1$, $\sigma = 1.0$. (a) $L = 4.0$, (b) $L = 16.0$.

essentially independent of the number of cells. Solution branches for larger values of n have saddle-node bifurcations at successively smaller values of Q/R .

6. Varying ζ

We have explored the region of (Q, ζ) parameter space for which convectons exist, both in the Boussinesq equations (2.1) - (2.3) and in the truncated model (2.6) - (2.10). The numerical simulations of the Boussinesq equations were carried out with a pseudospectral code due to Stephen Cox and Paul Matthews. Figure 9(a) shows that convectons exist in a region bounded, at large Q , by the saddle-node bifurcation, and, at small Q , by the two instabilities identified earlier; a subcritical (and symmetry-breaking) bifurcation that results in a $n = 2$ -roll localised state, and the linear instability of the outside region to weak oscillatory convection. Figure 9(b) shows the region of existence of convectons for the full 2D Boussinesq equations (2.1) - (2.3) for $R = 10000$. For $R = 5000$ in the Boussinesq equations the convectons exist over an extremely small region in parameter space. For $\zeta \approx 1$, in both the Boussinesq equations and the truncated model (2.6) - (2.10), the convectons exist over a small region of Q and are not completely localised, in the sense that small counter-rotating eddies appear on either side of the main cell. This is illustrated in figure 10 and was noted by Cox, Matthews and Pollicott (2004). Figure 10(b) illustrates that although the central convection cell remains fully field-free, the smaller cells do not. Because the approximate model discussed above assumes $\zeta \ll 1$ and assumes complete expulsion from every convection cell, it therefore does not describe these localised solutions at all accurately for $\zeta > 0.3$. For $\zeta > 0.3$ we find that convectons in the truncated model, figure 9(a), lose stability through a subcritical bifurcation in which additional strong convection cells appear. In the simulations using the 2D

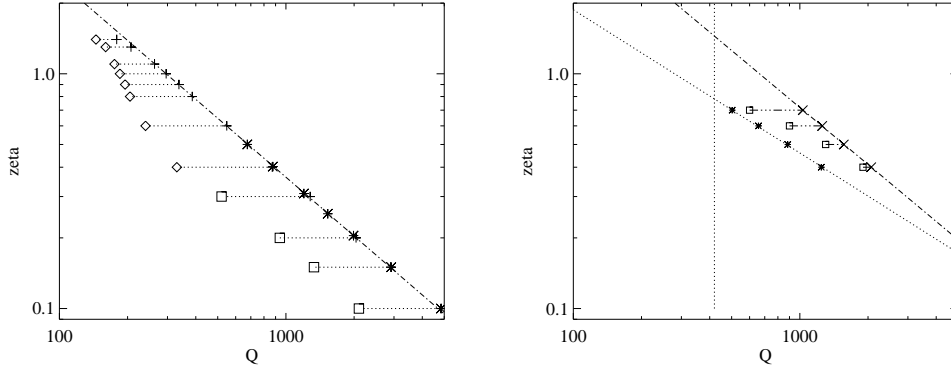


FIGURE 9. Location of single-roll convectons (\cdots) in the (Q, ζ) plane for $L = 6.0$: (a) obtained from numerical simulations and boundary-value solving of (2.6)-(2.10) for $R = 5000$. \diamond indicates subcritical instability, \square indicates oscillatory instability in the outside region, $+$ indicates saddle-node bifurcation located through timestepping, $*$ indicates saddle-node located by boundary-value solving. Dashed line indicates the power law $Q\zeta^{1.2} = 296$. (b) obtained from the full Boussinesq equations (2.1) - (2.3) for $R = 10000$. Dotted lines estimate the location of linear instabilities to weak convection in the outer region: vertical - steady instability, sloping - oscillatory instability. \square indicates oscillatory standing-wave instability, \times indicates saddle-node bifurcation, $*$ indicates approximate point of oscillatory instability in the outside region from linear theory.

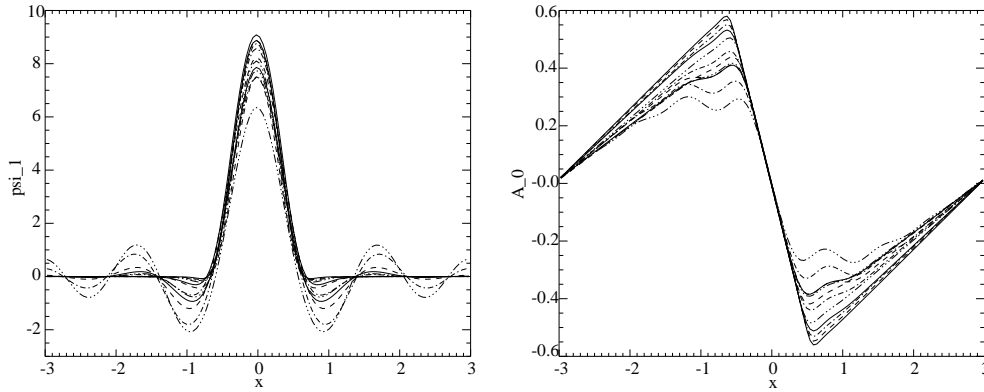


FIGURE 10. Evolution of convecton profiles with increasing ζ , from numerical simulations of (2.6) - (2.10). (a) ψ_1 , (b) A_0 . Plots are for (ζ, Q) pairs: (0.1, 4000), (0.15, 2400), (0.2, 1100), (0.3, 700), (0.4, 500), (0.6, 500), (0.8, 320), (0.9, 300), (1.0, 260), (1.3, 180), (1.4, 165). These points lie close to the line $Q\zeta^{1.2} = 250$, just below the saddle-node bifurcation line in figure 9(a).

Boussinesq equations, convectons lose stability in an oscillatory bifurcation, producing standing-wave oscillations, before the outside region becomes linearly unstable.

An intriguing feature of figure 9 is the precise power law scaling of the locations of the saddle-node bifurcation points. Figure 11 shows, moreover, that data for different values of R still collapse to a single power law. Figure 11 contains data from time integrations of both the truncated equations and the full Boussinesq equations. The location of each saddle-node point was carefully estimated from the time integrations by curve fitting to the solution amplitude, as measured, for example, the Nusselt number. The results obtained in this way for the truncated PDEs (2.6) - (2.10) are in excellent agreement

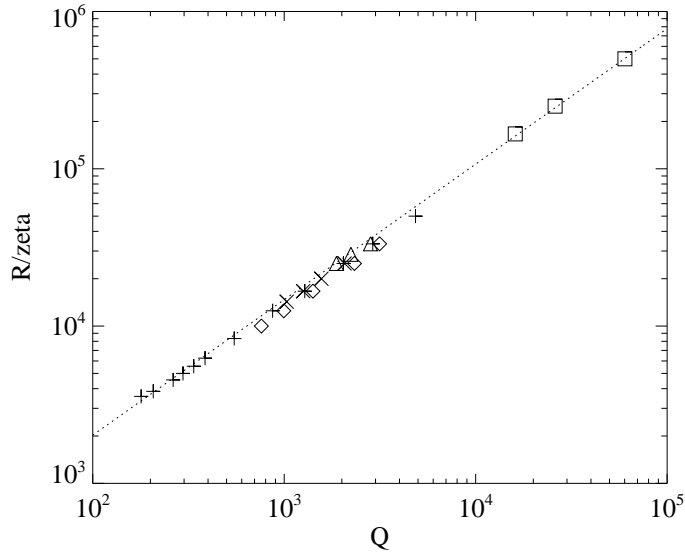


FIGURE 11. Data collapse for the location of the saddle-node bifurcation. Dotted line: best fit power law $R/\zeta = 38.2581 Q^{0.861758}$ for results at $L = 6.0$. +: $R = 5000$, $L = 6.0$, truncated PDEs; x: $R = 10000$, $L = 6.0$, 2D Boussinesq equations; \triangle : $R = 20000$, $L = 6.0$, 2D Boussinesq equations; \square : $R = 50000$, $L = 6.0$, truncated PDEs. \diamond : $R = 5000$, $L = 10.0$, truncated PDEs.

with solutions found by locating steady solutions of (2.6) - (2.10) as a boundary-value problem. The best fit power law to the data of figure 11 is

$$\frac{R}{\zeta} = 38.3 Q^{0.862}. \quad (6.1)$$

Not unexpectedly, for a fully nonlinear solution, the value of the exponent does not seem to correspond to any of the ‘obvious’ scalings motivated by linear theory and discussed by Julien et al. (1999) and Matthews (1999). The power law (6.1) cannot be deduced from the approximate model, which, as indicated by (4.5) always contains Q and R in the combination Q/R . It is of interest that R/ζ and Q are both proportional to $1/(\nu\eta)$ and are independent of the thermal diffusivity κ . The power law seems to hold without systematic deviation over a range of ζ and R . Figure 11 contains four data points for a domain size $L = 10.0$, indicated by the \diamond symbols. It appears that, although the constant of proportionality might depend weakly on L , the exponent does not.

It remains to comment on the degree to which the approximate model agrees with the 2D Boussinesq equations. Figure 12 shows the location of the saddle-node bifurcations from the 2D Boussinesq equations and from the approximate model, for $R = 50000$. Although the results are of the same order of magnitude, they clearly scale differently with ζ , showing the shortcomings of the approximate model.

7. Discussion and conclusions

In this paper we have constructed a simple model for the formation of localised convective states in the presence of a vertical magnetic field, motivated by the physics specific to this problem. The model predicts the existence of branches of solutions that are not related to the usual linear or weakly nonlinear theory, although one part of the approximate

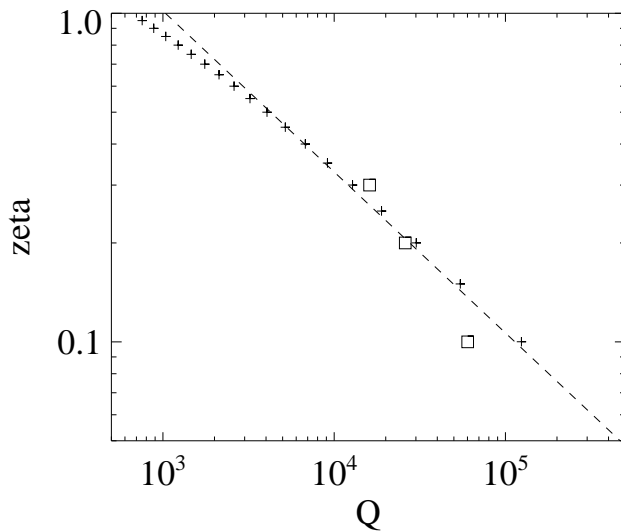


FIGURE 12. Comparison of the location of saddle-node bifurcations from the approximate model (+) and solutions of the 2D Boussinesq equations (\square) for $R = 50000$ and $L = 6.0$. Dashed line indicates the scaling law $\zeta \approx Q^{0.49}$.

model is essentially the Lorenz (1963) model for thermal convection in the absence of magnetic field. The inclusion of a horizontally-varying but z -independent mode $A_0(x)$ as well as the first Fourier mode $A_1(x)$ with vertical dependence $\cos \pi z$ enables the model to capture the flux expulsion effect identified by earlier authors, in particular Weiss (1966) and Knobloch et al. (1981). At leading order the model solution for $A_1(x)$ does not correspond to the usual eigenfunction for weakly nonlinear magnetoconvection in either the inside or outside regions. It is this lack of restriction of $A_1(x)$ to a sinusoidal form that is the essential structural difference between this model and the weakly nonlinear formulation analysed by Cox, Matthews and Pollicott (2004).

We compared the approximate model and our numerical results for the 2D Boussinesq equations and the Fourier mode truncation (2.6) - (2.10) with the numerical results of Blanchflower (1999a,b). The approximate model qualitatively explains and justifies much of the behaviour he observed; not only is the overall shape of the convectons broadly correct, but the existence and location of branches of these solutions, including those with more than one convection roll, arise naturally in the model. At fixed R there are upper and lower limits on the range of Q for which stable convectons exist. The upper limit is always in the form of a saddle-node bifurcation. The lower limit in Q is given either by the onset of weak oscillatory convection in the outer, quiescent, region, or by a subcritical bifurcation that creates additional vigorous convection cells. At lower ζ the oscillatory instability occurs first as Q is decreased. For fixed R and Q , there is a lower limit to the value of ζ for which convectons are stable, again, due to the occurrence of oscillatory convection in the outside region.

The approximate model makes use of the limits of small ζ , and large R and Q which, perhaps surprisingly, do not adversely affect each other. In the ‘inside’ region the limit $\zeta \ll 1$ enables the hydrodynamics to be decoupled from the magnetic field. From (3.7) it is seen that the effect of increasing R is to reduce the size of the $O(\zeta^3)$ correction

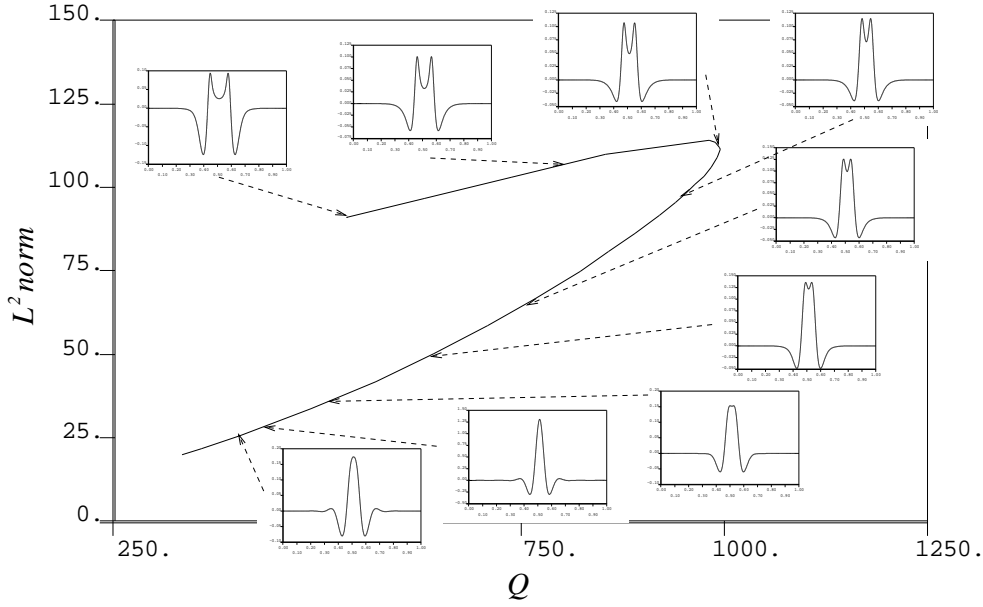


FIGURE 13. Evolution of the profile of $A_1(x)$ around the saddle-node bifurcation showing divergence from its form in figure 2 as the amplitude of the convection drops. Main figure shows solution amplitude as a function of Q for $R = 5000$, $L = 10.0$, $\zeta = 0.4$. Inserts show $A_1(x)$ with x rescaled to the unit interval, for $Q = 535, 855, 995$ (saddle-node point), $921, 769, 644, 492, 405$ and 357 .

term in relation to the leading order $O(\zeta)$ term, since $\hat{\psi}_0$ scales with $R^{1/2}$ for large R . In the ‘outside’ region the limit $Q = O(R)$, $R \gg 1$ enables the systematic determination of a balance between buoyancy and Lorentz forces. As noted in section 3.2.2 we assume also that $R^2\zeta \gg 1$; for typical values of R and ζ this forms little practical restriction. The limits used enable the leading-order forms of the streamfunction $\psi_1(x)$ and magnetic flux function variables $A_0(x)$ and $A_1(x)$ to be readily obtained. The main drawback is that the behaviour of the temperature variables is not incorporated, yet it is necessary to use the temperature variable θ_1 as one of the patching conditions. As a result the approximate model neglects nonlinear interactions between the thermal and velocity fields, and gives results that are not quantitatively correct for the parameter regime that is most easily accessible to numerical work. For large enough R and Q and small enough ζ , the approximate model yields results that are quite close to those of the 2D Boussinesq equations, as shown in figure 12, although there are clear systematic differences.

The most intriguing observation from the numerical investigations is the scaling law indicated in figure 11. There seems to be no immediate explanation for the exponent. It might be expected that the exponent tends to unity as the domain size L is increased, but the initial results for $L = 10.0$ in figure 11 show only weak dependence on L . More work is clearly needed on this point.

There are various directions in which future work on this problem could proceed. Firstly, it would be interesting to attempt to link this calculation to the weakly nonlinear theory developed by Cox, Matthews and Pollicott (2004). This should help to describe the ‘almost-localised’ states found at larger values of ζ , illustrated in figure 10. This figure also illustrates a potential problem with the existence of a ‘snaking’ sequence of

localised states with increasing numbers of vigorous convection cells, as explored in the papers by Sakaguchi & Brand 1996, Hunt et al. 2000 and Coulet et al. 2000: in the snaking scenario, one pair of these new small convection cells would develop into strong convection eddies as Q is decreased further, while the others would decay again as the solution ascended to the next turn of the snake. It remains possible, though, that the solutions for larger numbers of convectons link up in a ‘slanted snake’ with the saddle-nodes located at decreasing values of Q rather than tending towards a fixed value of Q as in the usual snaking diagram. Numerical solutions of the boundary value problem indicate that there may be some connection to ‘snaking’ since very small amplitude (and unstable) convectons resemble a localised version of the linear eigenfunction rather than preserving the overall form given by the approximate model for the large-amplitude convectons. This is illustrated in figure 13.

Secondly, it may be possible to extend the model to describe oscillatory convectons, which were found numerically by Blanchflower (1999a,b), and axisymmetric ones. An axisymmetric version of the vertically-truncated ODEs might help determine whether similar localised states are possible in three dimensions; certainly the physics would be the same even if the analytical effort required was substantially greater. This would help to shed further light on the interaction of thermal convection and magnetic fields in two and three dimensions.

I have been grateful for comments from Sean Blanchflower, John Lister, Paul Matthews, Alastair Rucklidge and the anonymous referees. Figures 1 and 8 are reproduced from Blanchflower (1999b) with the author’s permission. Financial support from Trinity College, Cambridge is gratefully acknowledged, as is the hospitality of the Isaac Newton Institute.

REFERENCES

- BATISTE, O. AND KNOBLOCH, E. 2005 Convectons. Preprint.
- BLANCHFLOWER, S.M. 1999a Magneto-hydrodynamic convectons. *Phys. Lett. A* **261**, 74–81
- BLANCHFLOWER, S.M. 1999b *Modelling Photospheric Magnetoconvection*. PhD thesis, University of Cambridge.
- BLANCHFLOWER, S.M., RUCKLIDGE A.M. AND WEISS N.O. 1998 Modelling photospheric magnetoconvection. *Mon. Not. R. Astron. Soc.* **301**, 593–608
- BLANCHFLOWER S.M. AND WEISS N.O. 2002 Three-dimensional magneto-hydrodynamic convectons. *Phys. Lett. A* **294**, 297–303
- BUSSE F.H. 1975 Nonlinear interaction of magnetic field and convection. *J. Fluid Mech.* **71**, 193–206
- CHANDRASEKHAR, S. 1961 *Hydrodynamic and Hydromagnetic Stability*. Oxford University Press.
- COULET P., RIERA C. AND TRESSER C. 2000 Stable static localized structures in one dimension. *Phys. Rev. Lett.* **84**, 3069–3072
- COX S.M. AND MATTHEWS P.C. 2001 New instabilities in two-dimensional rotating convection and magnetoconvection. *Physica D* **149**, 210–229
- COX S.M. AND MATTHEWS P.C. 2003 Instability and localisation of patterns due to a conserved quantity. *Physica D* **175**, 196–219
- COX S.M., MATTHEWS P.C. AND POLLICOTT S.L. 2004 Swift–Hohenberg model for magnetoconvection. *Phys. Rev. E*, **69**, 066314
- CROSS M.C. AND HOHENBERG P.C. 1993 Pattern formation outside of equilibrium. *Rev. Mod. Phys.* **65** 851–1112
- DOEDEL E., CHAMPNEYS A., FAIRGRIEVE T., KUZNETSOV Y., SANDSTEDTE B. AND WANG X. 1997 *AUTO97: Continuation and bifurcation software for ordinary differential equations*. Available via FTP from directory `pub/doedel/auto` at `ftp.cs.concordia.ca`
- HOYLE R.B. *Pattern formation: an introduction to methods* CUP. (2006)

- HUNT, G.W., PELETIER M.A., CHAMPNEYS A.R., WOODS P.D., WADEE M.AHMER, BUDD C.J. AND LORD G.J. 2000 Cellular buckling in long structures. *Nonlinear Dynamics* **21**, 3–29
- HURLBURT N.E. AND TOOMRE J. 1988 Magnetic fields interacting with nonlinear compressible convection. *Ap. J.* **327**, 920–932
- KNOBLOCH E., WEISS N.O. AND DA COSTA L.N. 1981 Oscillatory and steady convection in a magnetic field. *J. Fluid Mech.* **113**, 153–186
- KOMAROVA, N.L. AND NEWELL, A.C. 2000 Nonlinear dynamics of sand banks and sand waves *J. Fluid Mech.* **415**, 285–321
- JULIEN K., KNOBLOCH E. AND TOBIAS S.M. 1999 Strongly nonlinear magnetoconvection in three dimensions. *Physica D* **128**, 105–129
- LORENZ E.N. 1963 Deterministic nonperiodic flow. *J. Atmos. Sci.* **20**, 130–141
- MATTHEWS P.C. AND COX S.M. 2000 Pattern formation with a conservation law. *Nonlinearity* **13**, 1293–1320
- MATTHEWS P.C. 1999 Asymptotic solutions for nonlinear magnetoconvection. *J. Fluid Mech.* **387**, 397–409
- PROCTOR M.R.E. AND WEISS N.O. 1982 Magnetoconvection. *Rep. Prog. Phys.* **45**, 1317–1379
- ROTERMUND H.H., JAKUBITH S., VON OERTZEN A. AND ERTL G. Solitons in a surface reaction. *Phys. Rev. Lett.* **66** 3083–3086
- SAKAGUCHI H. AND BRAND H.R. 1996 Stable localized solutions of arbitrary length for the quintic Swift–Hohenberg equation. *Physica D* **97**, 274–285
- STRÜMPFEL C., PURWINS H.-G. AND ASTROV Y.A. Spatiotemporal filamentary patterns in a dc-driven planar gas discharge system. *Phys. Rev. E* **63** 026409
- SWIFT J.B. AND HOHENBERG P.C. 1977 Hydrodynamic fluctuations at the convective instability. *Phys. Rev. A* **15**, 319–328
- UMBANHOWAR P.B., MELO F. AND SWINNEY H.L. 1996 Localized excitations in a vertically vibrated granular layer. *Nature* **382**, 793–796
- WEISS, N.O. 1966 The expulsion of magnetic flux by eddies *Proc. R. Soc. Lond. A* **293**, 310–328
- WEISS, N.O. 1981a Convection in an imposed magnetic field. Part 1. The development of non-linear convection. *J. Fluid Mech.* **108**, 247–272
- WEISS, N.O. 1981b Convection in an imposed magnetic field. Part 2. The dynamical regime. *J. Fluid Mech.* **108**, 273–289
- WEISS, N.O. 2002 Umbral and penumbral magnetoconvection. *Astron. Nachr.* **323**, 371–376